Enhanced wear resistance, antibacterial performance and biocompatibility by nanotubes containing nano-Ag and silicate/phosphate on the surface of βTi alloy for bone application

Qingge Wang [a,1], Jia Liu [b,1], Hong Wu [a,*], Jingbo Liu [a], Yaojia Ren [a], Luxin Liang [c], Xinxin Yan [d], Ian Baker [e], Shifeng Liu [f], V.V.Uglov [g], Yujin Tang [b,*], Liqiang Wang [h,*]

[a] State Key Laboratory of Powder Metallurgy, Central South University, Changsha 410083, China

[b] Affiliated Hospital of Youjiang Medical University for Nationalities, Baise 533000, China

[c] Department of Orthopedics, The Second Xiangya Hospital, Central South University, Changsha 410011, China

[d] Department of Orthopedics, Renmin Hospital, Wuhan University, Wuhan 430060, China

e Thayer School of Engineering, Dartmouth College, Hanover, NH 03755-8000, USA

f School of Metallurgical Engineering, Xi'an University of Architecture and Technology, Xi'an 710055, China

g Tomsk Polytechnic University, Tomsk 634028, Lenina ave., 2a, Russia

h State Key Laboratory of Metal Matrix Composites, School of Material Science and Engineering, Shanghai Jiao Tong University, Shanghai 200240, China

[1] These authors contributed equally to this work.

*Corresponding author.

E-mail addresses:

hwucsu@csu.edu.cn; wuhong927@126.com (Hong Wu),

tangyujin196709@163.com (Yujin Tang),

wang_liqiang@sjtu.edu.cn (Liqiang Wang)

Abstract

An ideal Ti-based implant should avoid stress shielding surrounding the implants, besides a requirement of bioactivity. To achieve the requirements, Ti-35Nb-2Ta-3Zr (wt.%) alloy with a low elastic modulus was used as the substrate for the coatings to avoid stress shielding. The study constructed the micro/nano functional coatings containing bioceramics and Ag ion onto TiO_2 nanotubes by anodization, deposition and spin-coating methods. The tribocorrosion behavior, corrosion behavior, antibacterial activity and early osteogenic behavior of bioceramics (nano β-TCP, micro-HA and meso-$CaSiO_3$) and Ag nanoparticles coated on TiO_2 nanotubes *in vitro* were studied. Tribocorrosion and corrosion results exhibit the wear rate and corrosive rate was highly dependent on surface feature. The micro-structure could reduce wear tracks due to adhesive wear and abrasive wear. Compared with other scale structures, the nano-structured passive film showed higher density to prevent solution from corroding substrate. The meso-$CaSiO_3$ was favorable to the cell adhesion, proliferation and early differentiation. It is demonstrated that Si and P enhanced osteogenic response due to the micro/nano structure and ion releasing. Besides, the micro/nano coatings containing Ag ion exhibit great antibacterial capacity against *E. coli*. The findings indicated that hybrid coating can be a potential coating to accelerate osteogenesis process for orthopedic implants in clinic.

Keywords: β-Ti alloy; Surface modification; Wear resistance; Corrosion resistance; Osteogenic behavior; Antibacterial activity.

1. Introduction

Titanium alloys have been applied in the biomedical field for half a century because of high strength, low density and outstanding biocompatibility[1-5]. However, the mismatch of elastic modulus between titanium implant (~100 GPa) and the bone (15-30 GPa) induces stress shielding, even resulting in bone resorption and implant failure. To avoid the negative influence caused by stress shielding, novel β and near-β type Ti-based alloys with low elastic moduli (30-80 GPa) close to that of human bone have been developed [6-11]. To decrease elastic modulus for the better suitability, Ti-35Nb-2Ta-3Zr (TNTZ, wt.%) with elastic modulus of 48 GPa was developed [12, 13]. It has been reported that TNTZ was implanted in the iliac crests of goats for three weeks, which improved load transduction and bone remodeling in both new bone formation [14]. In another study, Zn nanoparticles was incorporated into TNTZ alloy by friction stir processing, reflecting great osteogenic differentiation and antibacterial properties (antibacterial rate: 83%)[15]. It has been investigated TiO_2 nanoparticles were doped into a TNTZ substrate, which improved the corrosion resistance in Hank's solution [16]. The above studies indicate that TNTZ after modification showed good corrosion resistance, antibacterial ability and osseointegration. Nevertheless, the bioactivity and wear resistance of TNTZ need to be further improved.

Surface modification is a common strategy to increase the bioactivity and wear resistance of titanium alloys[17-21]. Anodization is one of the representative surface modification technologies, which can introduce ordered TiO_2 nanotubes (TNTs) onto surfaces of titanium alloys by adjusting process parameters[22]. Yu et al. reported that larger TNTs improved the osteogenic differentiation by adjusting the diameter of nanotubes [23]. Recently, adding bioactive drugs into TNTs further improved the osteogenic properties. Alves et al. reported TNTs enriched with Ca and P to improve osteoblastic functions [24]. Zhang et al. developed the TNTs coatings co-doped Sr and Ca, promoting proliferation and osteogenic activities[25]. In Shen's study [26], TNTs doped dexamethasone and covered by chitosan multilayer films were designed,

reflecting great osteogenic behavior. Most of these studies focus on the osteogenic ability while neglect the antibacterial properties.

Ag plays a crucial part in antibacterial properties, and is one of the stable antibacterial agents. There have been studies about antibacterial mechanism of Ag NPs. Ag NPs are able to induce the bacteria to generate reactive oxygen species and eventually kill the bacteria[27]. Therefore, the amount of Ag doped is the key to achieve high antibacterial effect and keep low cytotoxicity. It is reported the antibacterial effect and cell activity of Ti-6Al-4V/Ag via friction stir processing was improved, when Ag content was 4.3-5.6%[28]. However, Ag appears obvious cytotoxicity above a certain dose[29]. It is necessary to control its release by designing a slow-release layer with bioactivity.

Bioceramics as a slow-release layer is an appropriate choice. In particular, the bioceramics can not only act as an ion release platform, but also be beneficial for osteogenic behavior. In Huang's study, hydroxyapatite (HA) layers containing Ag ion on porous structure provided a continuous Ag ion release kinetics platform, which showed great cell viability and had the positive effect on the formation of bone-like calcium sulphate[30]. It is reported that chitosan embedded Calcium silicate (CaSiO3) layers, as a drug release carrier, represented great biocompatibility, osteoconductivity, and degradability[31]. It is investigated that β-Tricalcium phosphate (β-TCP) coatings loaded Zn, Mg and Ti ions accelerated the bone healing process[32]. However, the release behavior of these three bioceramics to Ag ion still haven’t been clarified. After covering these bioceramics onto TNTs, the biological performance and wear mechanisms of also deserve to be investigated.

In this study, the bioceramics HA, $CaSiO_3$ and β-TCP with different particle sizes were coated onto TNTs loaded with Ag nanoparticles (Ag NPs). Both the wear behavior in simulated body fluid (SBF) and electrochemical behavior of the coatings have been investigated in detail. In addition, *in vitro* studies were performed to identify the osteogenic capacity (pre-osteoblasts adhesion, proliferation, and differentiation) and antibacterial properties of micro/nano coatings.

2. Materials and methods

2.1 Materials

Ti-35Nb-2Ta-3Zr (wt.%) plates measuring 10 mm × 10 mm × 1 mm were polished with 80, 400, 600, 1000, 1500, 2000, and 3000 grit sandpaper consecutively and then were cleaned with deionized water and ethanol (referred to as βTi). TNTs were fabricated on βTi substrate using an anodization device (Chroma, 62024P-600-8) for 30 min at 30 V DC in 0.1 M solution of HF, and then annealed for 2 h at 450°C [33] (referred to as TiNT). The TiNT was soaked in a 0.1 M solution of $AgNO_3$ in water for 10 min under UV radiation (365 nm wavelength) to incorporate Ag NPs (referred to as TiNTAg). The HA particles (10-100 μm), $CaSiO_3$ particles (>150 μm) and β-TCP particles (200-300 nm) were applied onto the TiNTAg by spin-coating at a speed of 3000 rpm for 20 s (referred to as TiNTAg@HA, TiNTAg@$CaSiO_3$, TiNTAg@β-TCP) [34]. The preparation process of the hybrid coating showed in Fig. 1a.

2.2 Microstructural Characterization

The phase analysis and microstructural characterization for the specimens were carried out via X-ray diffraction with Cu-Kα radiation at 40 kV and 40 mA with a step of 0.02°/s (XRD, D8 ADVANCE, Bruker), and a field electron gun scanning electron microscope at 5-20 kV (SEM, Quanta250FEG). The location of the Ag in TNTs was characterized by high-resolution transmission electron microscopy (HRTEM, FEI, Tecnai G2F20) and selected area electron diffraction (SAED).

2.3 Ag ion Release

The specimens were put in SBF solution at 37°C for various durations (6 h, 12 h, 1 day, 2 days, 3 days, 5 days, 7 days and 14 days), and the resulting ion release was measured using a plasma spectrometer (SPECTRO BLUE).

2.4 Tribocorrosion Tests

Tribocorrosion tests were carried out using a HT-1000 tribotester in a circular motion

in the SBF solution. The counterpart was 4 mm dia. GCr15 steel ball. Tests were performed with 4.9 N load for 1800 s, 4 mm sliding displacement, and 4 Hz frequency. The three-dimensional structure of the surface after the tribocorrosion test was characterized using super deep scene 3D microscope.

2.5 Corrosion Tests

Electrochemical measurements of the specimens were proceeded using a CS310OH electrochemical workstation in SBF solution using a three-electrode electrochemical cell with a saturated calomel electrode (SCE), reference electrode and a Pt foil electrode. When's open circuit potential (OCP) of the specimens became steady, electrochemical impedance spectroscopy (EIS) was carried out at frequencies from 10^{-2} to 10^{5} Hz at room temperature. The resulting data were analyzed using Zview 3.1 software. Potentiodynamic polarization curves were obtained at a sweep rate of 1 mV/s.

2.6 *In Vitro* Experiments

2.6.1 Cell culture

MC3T3-E1 cells (mouse embryo osteoblast precursor cells from China Infrastructure of Cell Line Sources) were incubated in an a-minimum essential medium (a-MEM) (Gbico, Invtrogen, Inc) containing 10% fetal bovine serum (FBS, Gibco, USA) and 1 % penicillin/streptomycin (PS, Life Technologies, USA) in an incubator (5 % CO_2, 100 % humidity, 37°C). The culture medium was replenished every 2 days.

2.6.2 Cell morphology

MC3T3-E1 cells were seeded onto the surfaces of specimens with a density of 5×10^4 cells per well. After incubating for 8 h and 24 h, the MC3T3-E1 cells were cleaned three times and were fixed with 2.5 % glutaraldehyde (Sigma, USA) in water for 12 h. Subsequently, the cells were dehydrated using ethanol at different concentrations of 30, 50, 70, 80, 90, 95 and 100 v/v % in PBS, and immersed into tertiary butanol solution at different concentrations of 25, 50, 75 and 100 v/v % in ethanol, each for 5 min. The specimens with cells were covered with gold before SEM observation.

2.6.3 Cell proliferation

A density of 2 × 10^4 MC3T3-E1 cells per well was seeded on the surfaces of specimens. After incubating for 1, 3, and 5 days, the cells were cleaned with PBS and immersed in 2 μM calcein-AM (Dojindo, Japan) for live cells after 30 min at 37°C. The images were recorded with a fluorescence microscope (DSYL140, Chang Heng Rong Technology, China).

2.6.4 Alkaline phosphatase (ALP) activity

MC3T3-E1 cells were introduced on the surfaces of the specimens with a cell density of 2 × 10^4 cells per well for 7 days to evaluate the ALP activity. For qualitative testing, cells were cleaned in PBS and fixed with 4 % paraformaldehyde (PFA) in water for 15 min at the specified time and stained by an ALP testing kit (Beyotime Biotechnology, China). Then, the stained specimens were observed by an inverted microscope (DSY-L140, Chang Heng Rong Technology) and an optical microscope (DM4000M, Leica). For quantitative testing, RIPA cell lysis buffer (Beyotime, China) was put to each well and reacted for 15 min. Afterward, the lysed solutions were centrifuged at 12,000 rpm for 10 min and detected via an ALP testing kit (Jiancheng bio-engineering research institute of Nanjing) by a microplate reader at 410 nm (Perkin-Elmer, USA). The ALP activity was standardized using the total protein content determined with a BCA assay kit (Beyotime, China) via a microplate reader at 570 nm.

2.6.5 Antibacterial activity

E. coli (ATCC25922) was used to evaluate the antibacterial activity of specimens. 1 mL bacterial broth with a concentration of 10^7 CFU/mL was seeded into each well of 24 well-plates and cultured for 12 h. The bacterial broth for blank group was diluted to 2000 CFU/mL and added 100 μL to LB solid medium for each group, respectively. The broth was spread evenly on the plates using a sterilized spatula, and then placed in the incubator for 12 h. The antibacterial rate can be calculated by the equation: Antibacterial rate = $(1-N_x/N_b) \times 100\%$, N_x and N_b represent the number of colonies on solid medium for each group.

2.6.6 Statistical analysis

All experiments were carried out in quadruplicate. The results were presented as the mean ± standard deviations (SD). The statistical significance was analyzed by a one-way ANOVA. Significant differences between specimens were shown as: *$p < 0.05$, **$p < 0.01$, and ***$p < 0.001$.

3. Results

3.1 Surface characterization

Fig. 1b-g shows SEM images of the specimens. Two different TNTs with diameters of approximately 70 nm and 180 nm distribute homogeneously. Fig. 1d-f reveals the specimens with HA, $CaSiO_3$, and β-TCP coated onto the TNTs and Ag NPs via spin-coating. Fig. 1g reflects the phase composition from the specimens. Peaks from both anatase (TiO_2) and β-Ti could be observed after annealing, indicating that the TNTs were transformed from amorphous into anatase. HA, $CaSiO_3$, and β-TCP peaks could be found in the patterns for the TiNTAg@HA, TiNTAg@$CaSiO_3$, and TiNTAg@β-TCP, respectively.

Fig. 1h shows Ag^+ concentration of the specimens. The Ag^+ concentration value was up to 0.85 mg/L in TiNTAg group. The cumulative Ag^+ concentrations were 0.54, 0.33 and 0.61 mg/L in the TiNTAg@HA, TiNTAg@$CaSiO_3$, and TiNTAg@β-TCP, respectively, suggesting that Ag^+ slow-release carrier was established by covering bioceramics. The total Ag^+ release was dominated by the dissolution of the TiNTAg.

To determine the distribution of Ag NPs in the TNTs, the TiNTAg is characterized by TEM analysis in Fig. 1i-m. As expected, Ag NPs presented inside TNTs (Fig. 1j-k). Ag NPs incorporated in TNTs were 30-70 nm in diameter. To identify the localization of Ag NPs, analysis of HRTEM image and SEAD pattern are carried in Fig. 1l-m. The crystalline structure of the Ag inside the TNTs was typical with an interplanar distance d_{hkl} (111) of 2.359 Å, corresponding to polycrystalline ring in Fig. 1m. Based on these results, it was confirmed that the Ag NPs were in a metallic state and the Ag NPs were embedded into nanotubes.

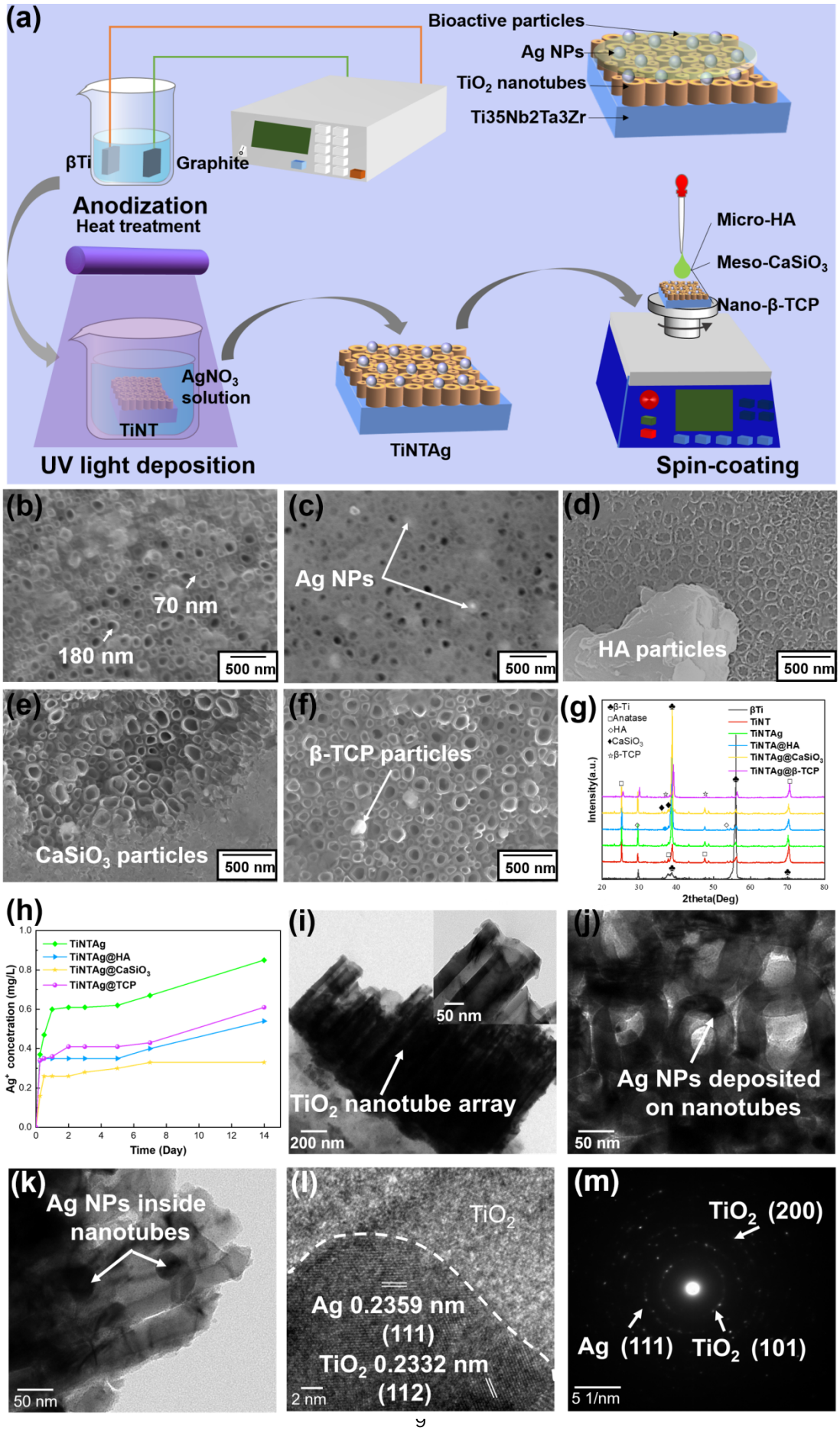

Fig. 1 (a) Schematic of the hybrid coatings preparation. SEM images of (b) TiNT, (c) TiNTAg, (d) TiNTAg@HA, (e) TiNTAg@$CaSiO_3$, (f) TiNTAg@β-TCP, (g) XRD patterns of the specimens. (h) Ag^+ release vs. time after immersion in SBF solution. TEM images of TiNTAg: (i) low magnification image, (j) top-view; (k) distribution and location of Ag NPs in the TNTs, (l) HRTEM image of Ag NP in (k), (m) SAED pattern of (l).

3.2 Tribocorrosion behavior

The wear interactions between a biomaterial and the surrounding tissue are crucial to implant lifetime. Fig. 2a shows the COFs for the βTi, TiNT, TiNTAg, HA, TiNTAg@HA, TiNTAg@$CaSiO_3$, and TiNTAg@β-TCP under tribocorrosion conditions for 1800s. For the substrate, the COF was 0.61. Initially, the COF of the TiNT was significantly lower but after a short period of time the COF sustained at 0.75. The COFs of the TiNTAg@HA, TiNTAg@$CaSiO_3$, and TiNTAg@β-TCP were low and stable for 600 s because of the bioceramics.

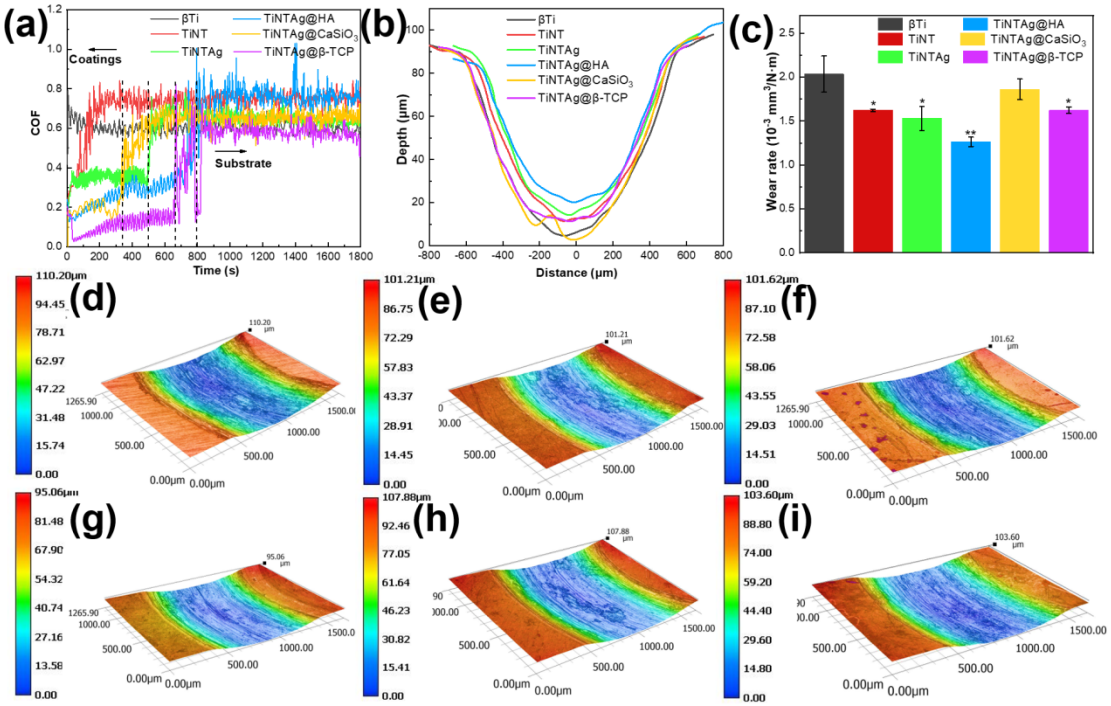

Fig. 2 (a) The COFs of specimens in SBF solution at 37 ± 0.5 °C under tribocorrosion (The dashed lines represent the failure point of different coatings during friction process.); (b) cross-sectional profiles of the wear tracks for each specimen; (c) wear rate under tribocorrosion conditions, 3D surface morphologies recorded after tribocorrosion tests for (d)βTi, (e) TiNT, (f)TiNTAg, (g)

TiNTAg@HA, (h)TiNTAg@CaSiO3, (i)TiNTAg@β-TCP. (*p < 0.05 and **p < 0.01 compared with the βTi group)

The wear rate ($mm^3/N \cdot m$) can be calculated by the wear tracks using equation[35]:

$$wear\ rate = \frac{V}{W \cdot L} = \frac{S \cdot C}{W \cdot 2\pi r \cdot n} \quad (1)$$

Where V is the volume loss; W is the normal load; L is the sliding distance; S is the cross-section area of worn surface; C is the sliding girth; r is sliding radius; and n is the wear circles. The cross-sectional profiles of the wear tracks can be observed in Fig. 2b. The wear tracks of the βTi and the TiNTAg@$CaSiO_3$ were the deepest with a maximum depth of ~90 μm. Among the specimens, the TiNTAg@HA had the shallowest track of ~60 μm under tribocorrosion condition. As seen in Fig. 2c, the wear rates of the βTi, TiNT, TiNTAg, TiNTAg@HA, TiNTAg@$CaSiO_3$, and TiNTAg@β-TCP in SBF solution are 2.03±0.24, 1.62±0.01, 1.53±0.13, 1.26±0.06, 1.86±0.11, 1.62±0.03 $\times 10^{-3}$ $mm^3/(N \cdot m)$, respectively. Notably, the TiNTAg@HA reveals the lowest wear rate, and the 3D surface morphologies also have proven the point (Fig. 2d-i).

Fig. 3 shows SEM images of the surfaces after the tribocorrosion tests. The wear track surface of the βTi is rather wide and deep, and micro ploughing can be observed clearly (Fig. 3a-b), accompanied by considerable plastic deformation. The wear tracks of the other specimens were shallow with the wear debris consisting of spalled coatings and oxide particles. In particular, the TiNTAg@HA showed the narrowest and shallowest wear track. It can be concluded that the TiNTAg@HA has the best wear resistance in contrast with the wear rate. The wear mechanism will be discussed in next section in Fig. 3m-n.

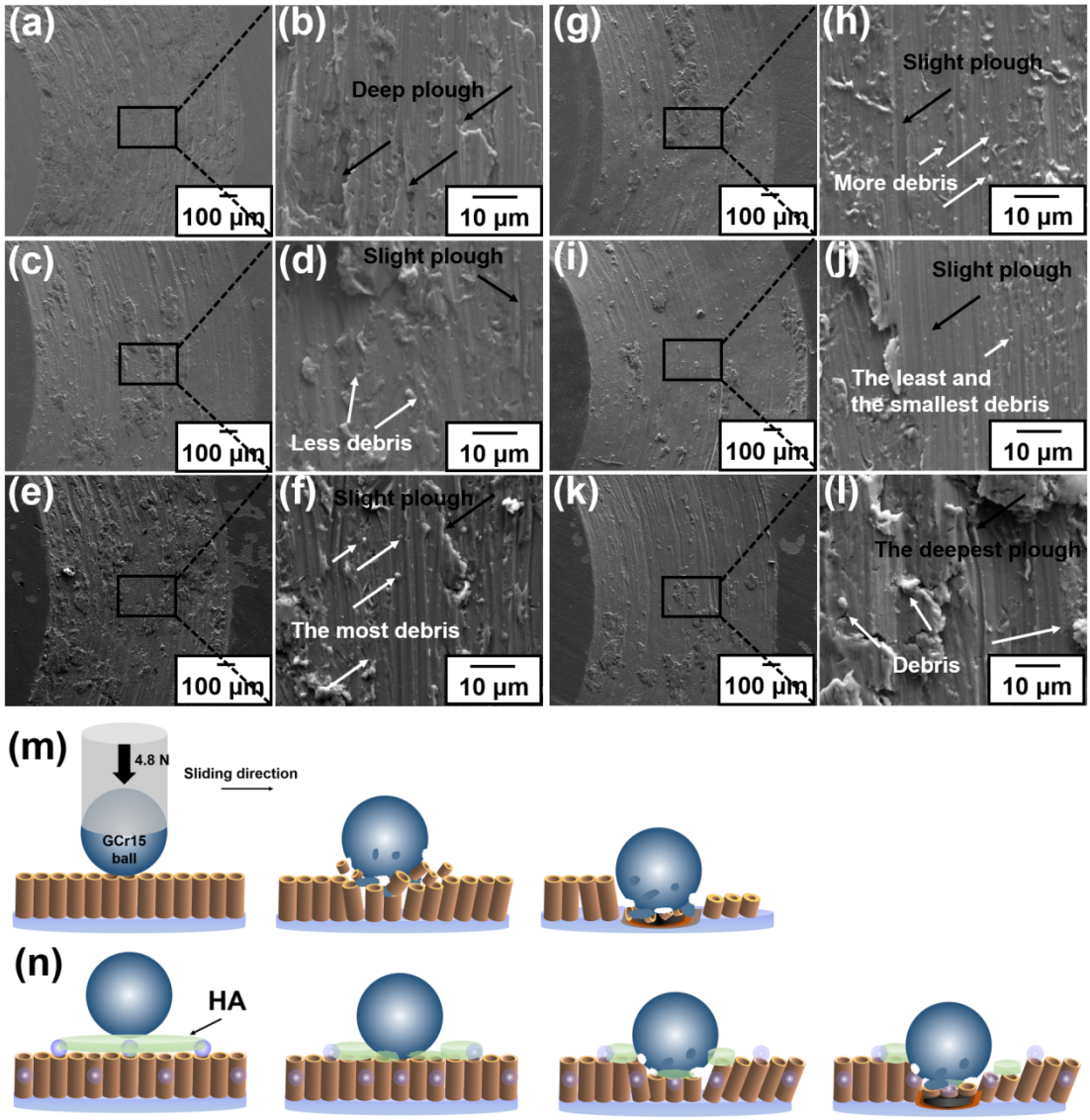

Fig. 3 SEM images of the wear tracks after tribocorrosion tests in a SBF solution for: (a-b) βTi, (c-d) TiNT, (e-f) TiNTAg, (g-h) TiNTAg@HA, (i-j) TiNTAg@$CaSiO_3$, (k-l) TiNTAg@β-TCP. Schematic of the tribocorrosion process of the (m) TiNT and (n) TiNTAg@HA in SBF solution.

3.3 Corrosion behavior

Fig. 4 reflects the electrochemical characteristics of all the specimens in SBF solution. To determine the corrosion process, potentiodynamic polarization curves of the βTi, TiNT, TiNTAg, TiNTAg@HA, TiNTAg@$CaSiO_3$ and TiNTAg@β-TCP are represented in Fig. 4a.

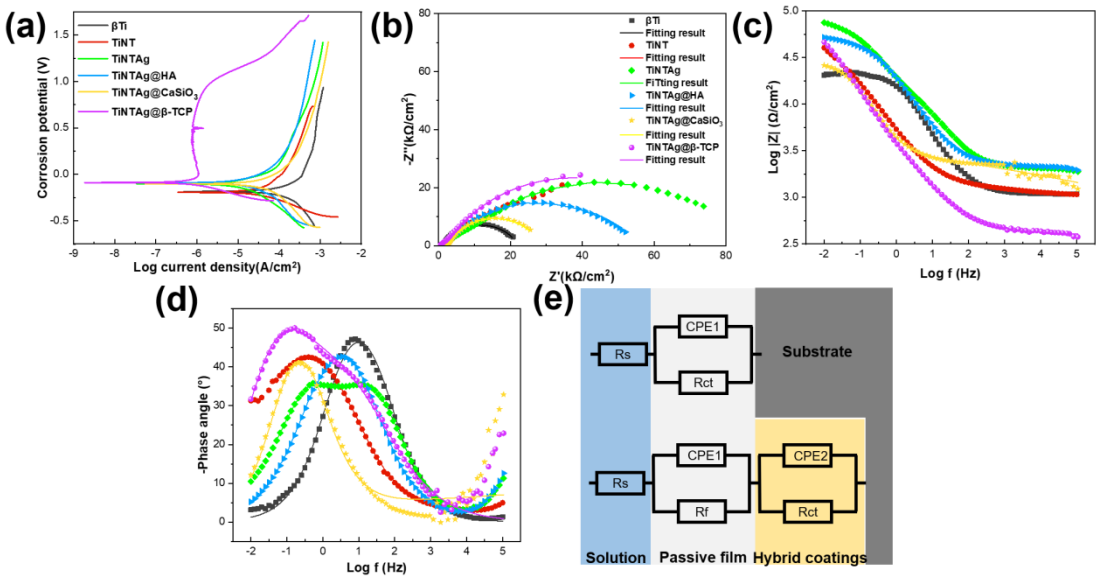

Fig. 4 Electrochemical results for various specimens in SBF: (a) Potentiodynamic polarization curves; (b) Nyquist plots; (c) Bode plots of log |Z| vs. frequency; (d) Phase angles vs. frequency; and (e) Equivalent electric circuit (EEC) for the specimens.

Table 1. Electrochemical parameters for various specimens in SBF solution.

Specimen	E_{corr} (V)	i_{corr} (mA)	MR (g/m^{2}d)	CR (mm/yr)
βTi	-0.18	0.105	28.02	1.64
TiNT	-0.19	0.040	10.55	0.62
TiNTAg	-0.10	0.013	3.37	0.20
TiNTAg@HA	-0.09	0.011	2.87	0.17
TiNTAg@$CaSiO_3$	-0.10	0.017	4.45	0.26
TiNTAg@β-TCP	-0.09	0.001	0.26	0.02

The E_{corr} and i_{corr} were obtained through Tafel extrapolation in Table 1. E_{corr} represents the degree of corrosive difficulty. Generally, the more positive the E_{corr} value, the greater the corrosion resistance. The TiNTAg@β-TCP showed a more positive E_{corr} in comparison to other specimens. The i_{corr} is related to the corrosion rate (CR) and the mass loss rate (MR). The lower the i_{corr} value, the stronger the corrosion resistance. The TiNTAg@β-TCP displayed the lowest i_{corr} of 0.96 nA. According to Faraday's Law, the specific CR (mm/yr), and the MR (g/m^{2}d) can be

calculated from [36]:

$$EW = \frac{1}{\sum \frac{n_i f_i}{W_i}} \quad (2)$$

$$CR = K_1 \frac{i_{corr}}{\rho} EW \quad (3)$$

$$MR = K_2 i_{corr} EW \quad (4)$$

Where K_1 = 3.27×10^{-3} mm g/μA cm yr; K_2 = 8.954 × 10^{-3} g cm^2/μA m^{2}d; i_{corr} represents the corrosion current density (μA/cm^2); ρ represents the density (g/cm^3); n_i represents the valence of the i^{th} element of the alloy; f_i represents the mass fraction of the i^{th} element in the alloy; and W_i represents the atomic weight of the i^{th} element.

Consequently, the βTi revealed the highest MR and CR (28.02 g/m^{2}d, 1.64 mm/yr), while the MR and CR of the TiNTAg@β-TCP was only 0.26 g/m^{2}d and 0.015 mm/yr.

Fig. 4b shows Nyquist plots of EIS spectra for the specimens. Corrosion resistance improved with increasing arc radius of the Nyquist plots. The arc radius values were ranked βTi < TiNTAg@$CaSiO_3$ < TiNTAg@HA< TiNT< TiNTAg < TiNTAg@β-TCP. The AC impedance at high frequencies revealed coating characteristics, while the AC impedance at the low frequencies reflected the double-layer capacitance C_{dl} and Faraday reaction resistance R_{ct} [37]. The Bode plots and phase angles plots in Fig. 4c-d show that the TiNTAg@β-TCP exhibits a higher |Z| and a higher phase angle with greater stability of the corrosion product passive film, and is far higher than those of βTi. At the high frequencies of 10^3-10^5 Hz, the phase angle values were close to 0° due to the response of electrolytic resistance. Yo sum up, the TiNTAg@β-TCP coating significantly increased the corrosion protection.

Table 2. EIS fitting parameters of each specimen in SBF solution.

specimen	R_s (Ω cm^2)	R_f (Ω cm^2)	CPE_1 (S cm^{-2} s^{-n})	n_1	CPE_2 (S cm^{-2} s^{-n})	n_2	R_{ct} (Ω cm^2)
βTi	11.1	-	9.54Í10^{-6}	0.75	-	-	2.17Í10^4

TiNT	14.0	1.57×10^{5}	6.83×10^{-4}	0.026	7.01×10^{-5}	0.62	5.70×10^{4}
TiNTAg	20.3	6.93×10^{3}	9.89×10^{-6}	0.70	2.02×10^{-5}	0.68	7.35×10^{4}
TiNTAg@HA	20.8	4.72×10^{4}	1.30×10^{-5}	0.69	6.1×10^{-4}	0.32	4.80×10^{4}
TiNTAg@$CaSiO_3$	22.7	4.48×10^{3}	1.02×10^{-4}	0.11	9.71×10^{-5}	0.81	3.46×10^{4}
TiNTAg@β-TCP	10.3	4.54×10^{4}	1.61×10^{-4}	0.49	1.20×10^{-4}	0.76	7.73×10^{4}

Table 2 lists EIS fitting results of each specimen in SBF solution. EEC are seen in Fig. 4e, where the upper part represents the equivalent circuit of the βTi, and the lower part reflects the equivalent circuit for the TiNT, TiNTAg, TiNTAg@HA, TiNTAg@$CaSiO_3$, and TiNTAg@β-TCP: R_s, R_f, *CPE*, and R_{ct} are the solution resistance, oxide film resistance, constant phase element, and charge transfer resistance, respectively.

3.4 Effect of coatings on MC3T3-E1 cells

3.4.1 MC3T3-E1 cells adhesion and proliferation

Fig. 5 shows the osteoblast shapes after 8 h and 24 h of incubation. Specifically, cells adhered to the βTi surface in a spindle shape. It was slightly improved on the TiNT surface, reflecting that more cells spread over a larger area. However, the number of MC3T3-E1 cells substantially reduced on the TiNTAg surface due to the Ag NPs toxicity leading to oxidative stress[38]. Cell spreading on the surfaces of the TiNTAg@HA, TiNTAg@$CaSiO_3$, and TiNTAg@β-TCP significantly increased in a polygonal osteoblastic shape and a larger area.

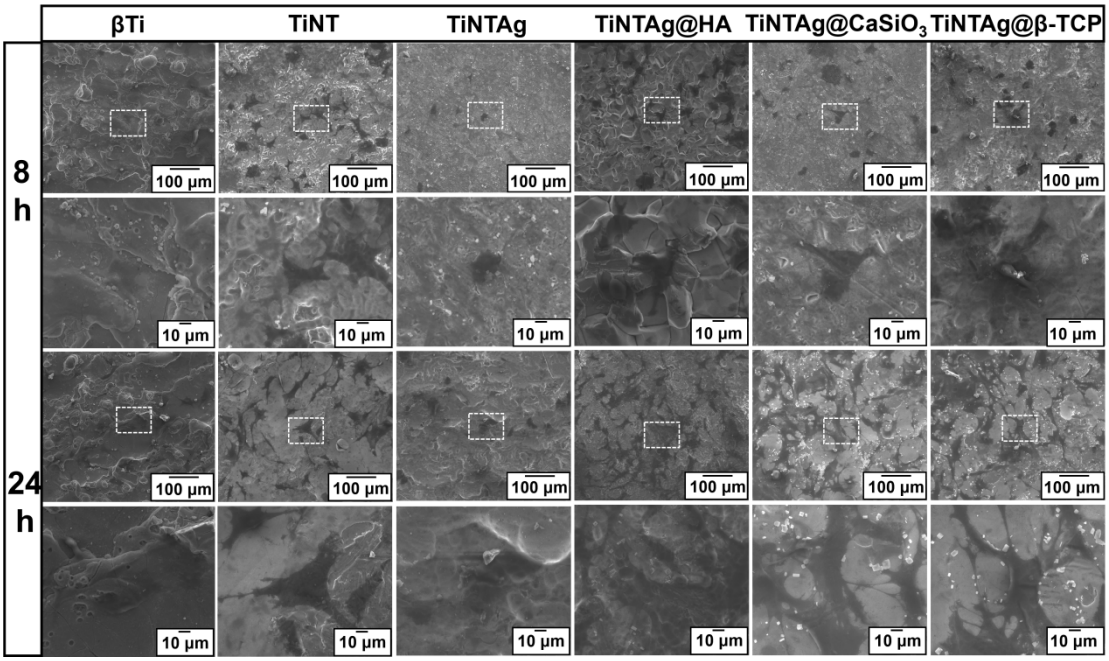

Fig. 5 SEM images of MC3T3-E1 cells on the specimen surfaces after 8 h and 24 h of incubation.

To ensure the survival condition of MC3T3-E1 cells, Fig. 6 shows fluorescent staining images after 1, 3 and 5 days of incubation. After culturing for 3 and 5 days, live cells for all specimens except for the TiNTAg exhibit remarkable increase, indicating the great cell proliferation ability. Particularly, the cells number of the TiNTAg@HA, TiNTAg@$CaSiO_3$, and TiNTAg@β-TCP represented significantly higher adhesion and proliferative capacity compared with the βTi, indicating that the presence of bioceramics can promote the cytocompatibility.

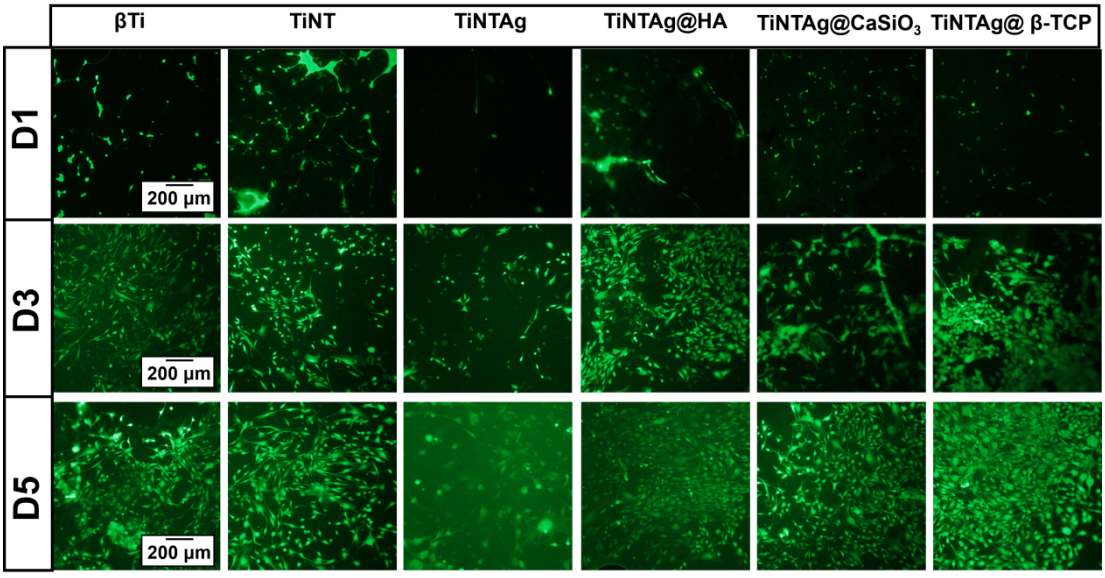

Fig. 6 Optical fluorescent images after 1, 3, and 5 days of incubation of MC3T3-E1 cells on

different specimens (scale bar: 200 μm) for live cells.

3.4.2 MC3T3-E1 cells differentiation

Fig. 7 reveals the qualitative and quantitative results of the ALP activity of MC3T3-E1 cells. The ALP activity of the specimens followed the trend: TiNTAg@$CaSiO_3$ > TiNTAg@HA > TiNTAg@β-TCP > TiNT > βTi > TiNTAg. Compared with the βTi, all the specimens show improvement in terms of ALP activity except for the TiNTAg. It is obvious that TiNTAg@$CaSiO_3$ improve osteogenesis *in vitro* by promoting ALP activity significantly.

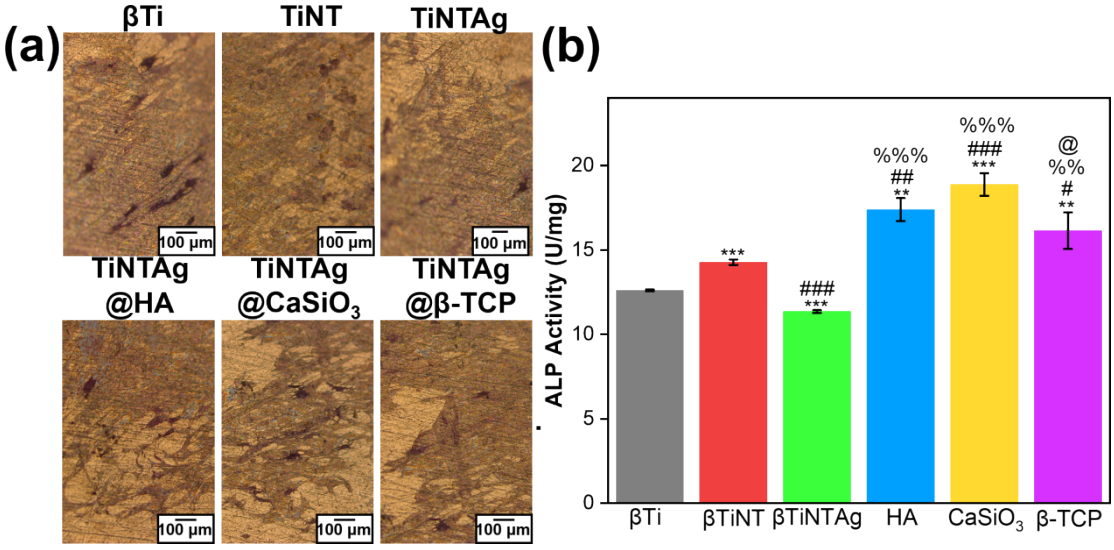

Fig. 7 Optical micrographs of ALP activity of MC3T3-E1 cells incubated for 7 days (a) qualitative results, (b) quantitative results. (*p < 0.05, **p < 0.01 and ***p < 0.001 compared with the βTi, #p < 0.05, ##p < 0.01 and ###p < 0.001 compared with the TiNT, %p < 0.05, %%p < 0.01, %%%p < 0.001 compared with the TiNTAg, @p < 0.05 compared with the TiNTAg@$CaSiO_3$.)

3.5 Antibacterial capacity

Fig. 9 shows the antibacterial results against *E. coli*, suggesting that the number of bacterial colonies significantly reduced compared with the βTi and TiNT groups. It is worth noting that the groups containing Ag show excellent antibacterial activity (antibacterial rate>90%). Meanwhile, there is no significant difference for the TiNTAg, TiNTAg@HA, TiNTAg@CaSiO3, and TiNTAg@β-TCP. The results reflect efficient antibacterial behavior of Ag NPs. The antibacterial mechanism of Ag

NPs can be found in our previous study[34].

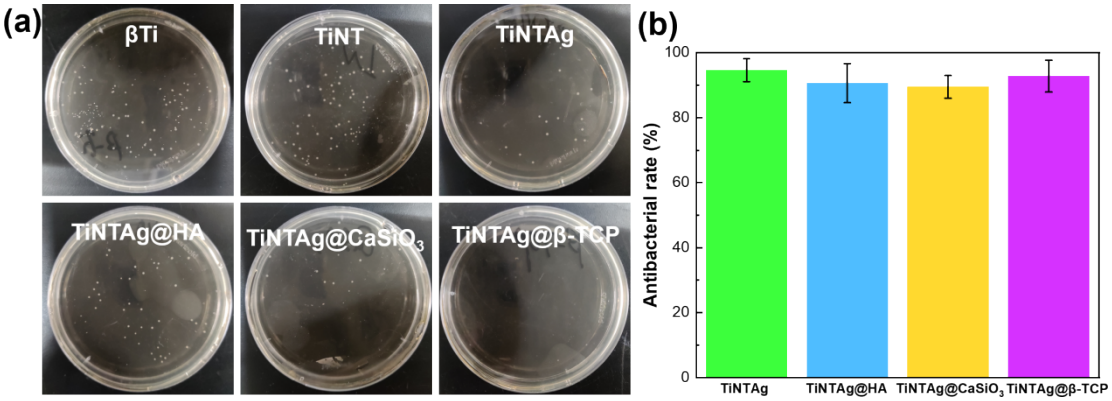

Fig. 8 (a) *E. coli* colonies on agar plates after 12 h incubation for each group, (b) The inhibition rates against *E. coli*.

4 Discussion

4.1 Wear behavior

Friction and wear are important factors during metal-to-bone contact in the osseointegration process. The tribocorrosion resistance depends on their surface characteristics, especially the surface coating. However, the effects of the COF under purely mechanical wear and tribocorrosion are different. Some studies reported the COF of Ti alloys were higher under tribocorrosion than that undergoing purely mechanical wear because the fluid environment accelerated the wear loss [35, 39]. Meanwhile, the coatings were corroded leading to increasing frictional forces under tribocorrosion, causing more wear loss[34]. In this study, the COF under tribocorrosion conditions were higher than those undergoing purely mechanical wear condition, see Fig. 2a and our previous work[34]. A similar phenomenon were observed in Xu's studies [39], which confirmed that during tribocorrosion the COF of Ti-16Mo and Ti-Mo-Cu were higher than those obtained in dry wear conditions.

To further clarify the tribocorrosion mechanism, the wear track surface morphologies are discussed. The wear tracks of the βTi showed irregular and deep ploughing lines along the direction of the circle because the third body debris of TNTZ alloy were incorporated in the contact region and moved with the counterpart

[40, 41], see in Fig. 3a-b. This can be attributed to the high hardness of GCr15. Severe plastic deformation is observed along the tracks due to TNTZ debris spalling pits, wear debris, and scratches subjected to high and continuous squeezing force in the edge area. Based on this evidence, the wear mechanism of the βTi involves abrasive wear during the tribocorrosion process.

As shown in Fig. 3c-d, the TiNT presents the slighter ploughing lines due to plastic deformation and less debris than in the βTi. Meanwhile, the TNTs were crushed between the TiO_2 debris and the TNTZ substrate, where the TiO_2 debris acted as the third-body wear debris [42]. The middle region in Fig. 3d indicated that the main behavior was trending to TNTs smashing and densification in the top zone, resulting in delamination and even detachment of the TNTs and forming wear debris under the continuous tangential friction force and normal load[43]. The wear debris was compressed to form a plastically-deformed hardened coating that protected the substrate. The TiO_2 debris accelerated the abrasive wear and caused small scratches. The dynamic pressure lubrication effect decreased the normal pressure and improved the anti-adhesive wear property. Moreover, TNTs enhanced the hydrophilicity and held fluid at the interface. TNTs covering the substrate lead to thicker lubrication, which turned boundary lubrication into fluid lubrication. To summarize, the schematic of wear process for the TiNT is demonstrated in Fig. 2m, which can be divided into three phases, i.e., partial crushing, full densification, and failure.

The wear rates of the TiNTAg@HA, TiNTAg@$CaSiO_3$, and TiNTAg@β-TCP showed difference significantly. The reason was both HA (10-100 μm) and β-TCP (200-300 nm) particles contained dispersed nano and microparticles, while the $CaSiO_3$ powder (>150 μm) was inhomogeneous and consisted of agglomerated large particles. After coating with HA, $CaSiO_3$, and β-TCP particles, different structures dominated the wear processes (Fig. 2n). For the TiNTAg@HA, the HA particles, as a barrier, protected the TNTs from the shear force generated by the pressure and lateral friction and delayed the damage of the nanotubes. Meanwhile, the microbar rolled at the interface of the counterpart and the TNTs produced a slight plough, thereby

producing the lowest wear rate (Fig. 3e-f). However, the 300 nm β-TCP particle debris, could not be pressed into nanotubes and instead stuck to the GCr15 ball, which prevented the counterpart from moving. This led to deep ploughing in the wear tracks (Fig. 3k-l). The $CaSiO_3$ particles accelerated destruction of the TNTs because of its large size. In the final stage of the wear process, all the three specimens involved partial densification and total densification at the top of the nanotubes and then failure. Eventually, the substrate was exposed while the counterpart made contact with the substrate.

4.2 Corrosion behavior

The corrosion behavior mainly depends on the passive films preventing liquid from penetrating into the substrate. The passive films on the surface of titanium alloys are susceptible to pH variations and surface wear. Toxic ions can be released into regions surrounding implants, and end up in the blood, urine and organs, which may damage cell functions and provoke immune response. To endow TNTZ with better corrosion resistance, specific coatings can be applied to the surface as a barrier to reduce the corrosion rate. In this study, the micro/nano coatings have shown significant improvements to the CR of the substrate. Hence, it is of great interest to clarify how the β-TCP particle-doped TNTs improve the corrosion behavior when subjected to SBF.

In general, there are three main factors that can improve the functionality of passive films, including the thickness of the oxide films, the composition of the oxide films, and the structure of the oxide films [16]. The electrochemical behavior of the specimens was investigated in SBF (Fig. 4). In spite of the formation of oxide film on the substrate, it was difficult for the thin and loose oxide film to inhibit corrosion. The βTi plate shows a typical equivalent electric circuit, which can be described as $R_s(CPE_1R_{ct})$ in Fig. 4e. R_{ct} reflects the ease of electrode process that the transition of charge goes through the interface between electrode and electrolyte solution. In contrast, the R_{ct} of all modified composites exhibited higher values than the substrate (Table 2).

Besides, almost all surface modification nanocomposite promotes cathodic

reactions on the surface of nanotube and nano-microparticles coatings leading to a positive shift in the E_{corr} (Fig. 4a and Table 1). Meanwhile, the corrosion current density of the anodic polarization curve decreased several orders of magnitude with the incorporation of particles. Mazare et al. [44] investigated that the corrosion resistance of TNTs improved with increasing annealing temperature from 350℃ to 750℃, which was correlated with the rutile content. In another study, it was demonstrated that corrosion protection of a TNTs coating reduced with increasing anodization voltage from 10 V to 50 V [45]. In this study, the TNTs present outer tube films and inner barrier films. Hence, the EEC of the TiNT can be described by $R_s(CPE_1R_f)(CPE_2R_{ct})$ with two-time constants, where CPE_2 and R_f represent the TNTs film and oxide film resistance at high frequencies. CPE_1 and R_{ct} reflect the double-layer capacitance and charge transfer resistance at low frequencies [37]. Hence, TNTs show better corrosion resistance than that of the βTi, which is in agreement with other studies [44, 46].

It is notable that the passivation zone appeared at the i_{corr} of 10^{-6} A/cm^2 for the TiNTAg@β-TCP, corresponding to a higher |Z| and a higher phase angle, as shown in Fig. 4. A passive region that extended over a wide potential range, suggesting rapid passivation behavior for the TiNTAg@β-TCP. This phenomenon primarily depends on the fast blockage of the current supplied by the β-TCP particles. The equivalent circuit for the β-TCP nanocomposite can be described by $R_s(CPE_1R_f)(CPE_2R_{ct})$. Significantly lower i_{corr} and R_{ct} values were observed for the TiNTAg@β-TCP indicating the superior corrosion resistance (Table 1-2), which is in agreement with an earlier study on Ca/P-doped TNTs [24]. The abrupt reduction of i_{corr} and the increase of Rct depends on the barrier film at the interface between the TNTs and the β-TCP nanoparticles. The β-TCP nanoparticle as an additional dense coating on the TNTs hindered the charge transfer resistance. In other words, the circuit required more charges involved in the process to provide better corrosion resistance. Therefore, the great corrosion resistance of the TiNTAg@β-TCP can be ascribed to the nanocomposite β-TCP, leading to higher density of the coating to avoid SBF damage.

Thus, great corrosive resistance is related to the density of the passive film. This knowledge is helpful for clarifying the fundamental reason behind the corrosion resistance improvement of the TiNTAg@β-TCP.

4.3 Cell response

As we known, cell behavior depends on the surface feature and chemical composition[22]. Osteoblast adhesion is the first step of material surface interactions, which affects cell proliferation and cell differentiation.

Generally, high cytotoxicity can be attributed to metal ion release. It was found that TNTZ, TNTs, Ag NPs and β-TCP have no detectable cytotoxicity to bone marrow mesenchymal stem cells (BMSCs)[34]. Cytotoxicity from Ag ion can be avoided by setting slow-release layer and preventing the Ag^{+} concentration (HA: 0.54 mg/L, $CaSiO_3$: 0.61 mg/L, and β-TCP: 0.33 mg/L) from reaching concentration threshold of 0.66 mg/L [47]. In particular, the Ca^{2+} and anions released from the specimen surface showed vital effect on proliferation of MC3T3-E1 cells. More MC3T3-E1 cells adhered on the TiNTAg@HA, TiNTAg@$CaSiO_3$, and TiNTAg@β-TCP surfaces while less cells adhered on the TiNTAg after early-incubation (8h and 24h) and mid-incubation (1, 3, and 5 days) times. These studies are in good accordance with other data [48-50].

ALP activity in osteoblasts is an early biochemical symbol [25, 51, 52]. High levels of ALP activity can induce the initial mineralization and further growth of hydroxyapatite crystals [53]. In this study, Si-loaded coatings displayed the most positive ALP activity compared with the TiNTAg@$CaSiO_3$. The finding maybe caused by the SiO_3^{2-} release of TiNTAg@$CaSiO_3$, which plays a role in growth factor to MC3T3-E1 cells. Thus, Si was favorable to the MC3T3-E1 cells in the early growth [31]. In a study of Ando et al.[54], the incorporation of Si showed a positive effect on osteoblast proliferation and the expression of TGF-b mRNA in human osteoblasts. For another study [55], $CaSiO_3$ promoted the formation of new bone. It is investigated that Si induced the osteoblast proliferation and the formation of the bone extracellular matrix[30]. In this study, it could be obviously seen that cell growth has no

cytotoxicity and has good osteogenic performance on the $CaSiO_3$ surface. In addition, the incorporation of $CaSiO_3$ into TNTs can transform the surface characteristics, leading to particular signals responsible for up-regulating some cell functions, and improving cellular adhesion, proliferation, and differentiation. Fig. 9 exhibits the interaction of MC3T3-E1 cells behavior and bioceramics. After contacted with micro/nano surface, MC3T3-E1 with a spindle shape and good outstretched filopodia spread to a larger area. The Ca^{2+} and anions including PO_4^{3-} and SiO_3^{2-} released from the particles. These ions entered cells through cell membrane channels, which caused up-regulation of ALP activity.

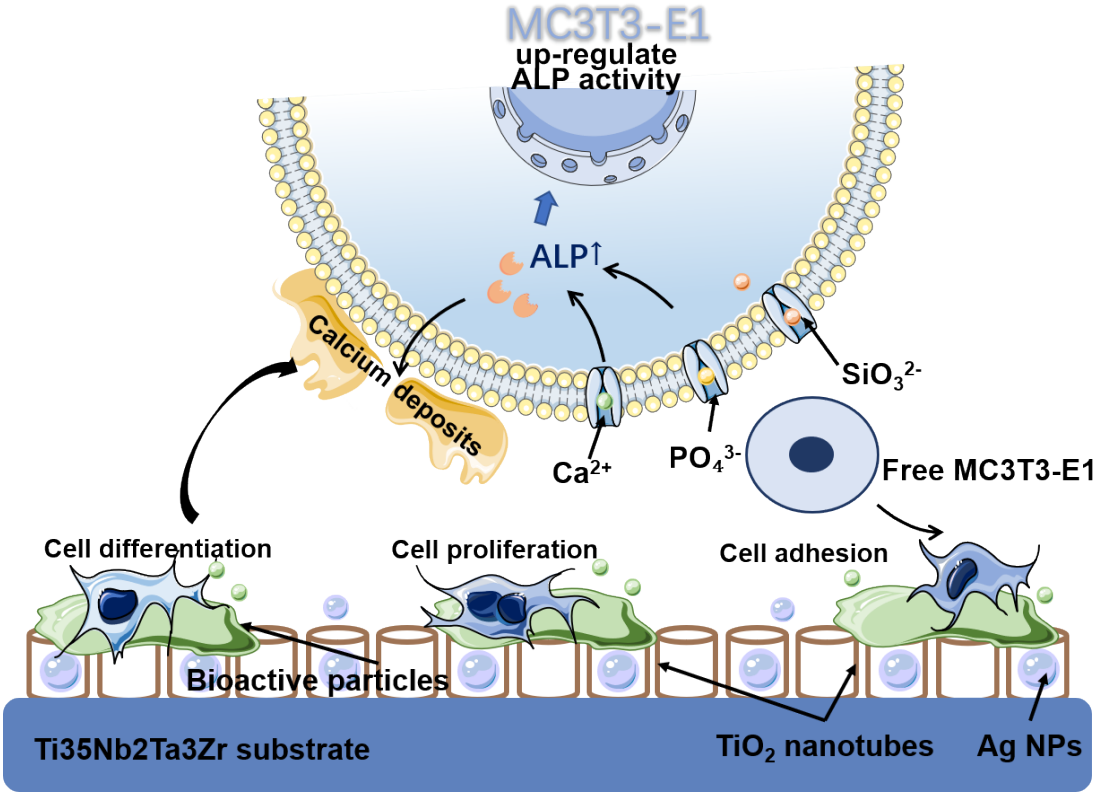

Fig. 9 Schematic of MC3T3-E1 cell growth on the specimen.

As mentioned, the osteogenic behavior depends on surface feature and chemical composition, which played a key role in promoting cell response and enhancing bone to implant interactions. The typical features (micro-HA, meso-$CaSiO_3$ and nano β-TCP particles) and released mineral ions (Si and P) from the hybrid coatings can promote osteoblast differentiation.

5. Conclusion

In this study, the micro/nano coatings containing bioceramics (nano β-TCP, micro-HA and meso-$CaSiO_3$) and Ag NPs were doped on the TNTs using anodization, deposition and spin-coating methods. The effects on wear, corrosion resistance and bioactivity for multi-scale structure were studied. After coated bioceramics, the Ag^+ release was controlled within the safety threshold. The micro-HA coating covered on TNTs reveals substantial tribocorrosion resistance, the wear mechanism is the combination of adhesive and abrasive wear (including the third body abrasion). The nano β-TCP coating shows excellent corrosion resistance, reflecting that passive film of the TiNTAg@β-TCP group is compact to impede the charge transfer resistance. The micro/nano structure and the incorporation of Si and P improve the processes of the adhesion, proliferation and early differentiation of MC3T3-E1 cells. Ag NPs endowed antibacterial properties to the coatings. The hybrid coatings including bioceramics and Ag NPs improved wear resistance, antibacterial capacity and increased cell response. Hence, the multi-scale coating is a promising biomaterial to control and adjust the surface structure and composition for improving comprehensive performance.

Declaration of Competing Interest

The authors declare no competing financial interest.

Acknowledgments

This work was supported by the National Natural Science Foundation of China (Grant Nos. 52071346, 52111530193), Hunan Provincial Natural Science Foundation of China (2021JJ30846), the Fundamental Research Funds for the Central Universities of Central South University (2022ZZTS0402). The authors would also thank Sinoma Institute of Materials Research (Guang Zhou) Co., Ltd. for the assistance with the TEM characterization.

References

[1] M. Wang, F. Bu, C. Zhou, Q. Zhou, T. Wei, J. Liu, W. Zhai, Journal of Micromechanics and Molecular Physics, 05 (2020) 2050016.

[2] T. Zhang, C.T. Liu, Advanced Powder Materials, 1 (2022) 100014.

[3] X. Li, Q. Huang, L. Liu, W. Zhu, T.A. Elkhooly, Y. Liu, Q. Feng, Q. Li, S. Zhou, Y. Liu, H. Wu, Colloids and Surf. B Biointerfaces, 171 (2018) 276-284.
[4] L. Guo, S. Ataollah Naghavi, Z. Wang, S. Nath Varma, Z. Han, Z. Yao, L. Wang, L. Wang, C. Liu, Materials & Design, 216 (2022) 110552.
[5] X. Lan, H. Wu, Y. Liu, W. Zhang, R. Li, S. Chen, X. Zai, T. Hu, Materials Characterization, 120 (2016) 82-89.
[6] D. Cai, X. Zhao, L. Yang, R. Wang, G. Qin, D.-f. Chen, E. Zhang, Journal of Materials Science & technology, 81 (2021) 13-25.
[7] J.C. Wang, Y.J. Liu, S.X. Liang, Y.S. Zhang, L.Q. Wang, T.B. Sercombe, L.C. Zhang, Journal of Materials Science & Technology, 105 (2022) 1-16.
[8] J. Hu, Y. Ren, Q. Huang, H. He, L. Liang, J. Liu, R. Li, H. Wu, Coatings, 11 (2021) 597.
[9] Z. Chen, Y. Liu, H. Wu, W. Zhang, W. Guo, H. Tang, N. Liu, Applied Surface Science, 357 (2015) 2347-2354.
[10] T. Zhang, D. Wei, E. Lu, W. Wang, K. Wang, X. Li, L.-C. Zhang, H. Kato, W. Lu, L. Wang, Journal of Micromechanics and Molecular Physics, 131 (2022) 68-81.
[11] Y. Ren, B. Han, H. Wu, J. Wang, B. Liu, B. Wei, Z. Jiao, Scripta Materialia, (2022).
[12] Y. Guo, D. Chen, W. Lu, Y. Jia, L. Wang, X. Zhang, Biomed. Mater, 8 (2013) 055004.
[13] L. Shao, Y. Du, K. Dai, H. Wu, Q. Wang, J. Liu, Y. Tang, L. Wang, Coatings, 11 (2021) 1446.
[14] C. Mao, W. Yu, M. Jin, Y. Wang, X. Shang, L. Lin, X. Zeng, L. Wang, E. Lu, Bioactive Materials, 16 (2022) 15-26.
[15] Y. Fang, Q. Wang, Z. Yang, W. Yang, L. Wang, J. Ma, Y. Fu, Materials & Design, 221 (2022).
[16] H. Gu, Z. Ding, Z. Yang, W. Yu, W. Zhang, W. Lu, L.-C. Zhang, K. Wang, L. Wang, Y. Fu, Materials & Design, 169 (2019) 107680.
[17] Q. Huang, X. Li, T. Liu, H. Wu, X. Liu, Q. Feng, Y. Liu, Applied Surface Science, 447 (2018) 767-776.
[18] W. Liu, L. Liang, B. Liu, D. Zhao, Y. Tian, Q. Huang, H. Wu, Colloids Surf. B Biointerfaces, 205 (2021) 111848.
[19] X. Li, Q. Huang, T.A. Elkhooly, Y. Liu, H. Wu, Q. Feng, L. Liu, Y. Fang, W. Zhu, T. Hu, Biomed Mater, 13 (2018) 045013.
[20] Q. Huang, X. Li, T.A. Elkhooly, S. Xu, X. Liu, Q. Feng, H. Wu, Y. Liu, Colloids Surf. B Biointerfaces, 169 (2018) 49-59.
[21] Q. Huang, X. Li, T.A. Elkhooly, X. Liu, R. Zhang, H. Wu, Q. Feng, Y. Liu, Colloids Surf. B Biointerfaces, 170 (2018) 242-250.
[22] Q. Wang, P. Zhou, S. Liu, S. Attarilar, R.L. Ma, Y. Zhong, L. Wang, Nanomaterials, 10 (2020) 1244.
[23] W. Yu, C. Qian, X. Jiang, F. Zhang, W. Weng, Colloids Surf B Biointerfaces, 136 (2015) 779-785.
[24] S.A. Alves, S.B. Patel, C. Sukotjo, M.T. Mathew, P.N. Filho, J.P. Celis, L.A. Rocha, T. Shokuhfar, Applied Surface Science, 399 (2017) 682-701.

[25] Y. Zhang, K. Wang, Y. Song, E. Feng, K. Dong, Y. Han, T. Lu, Applied Surface Science, 528 (2020) 147055.
[26] K. Shen, Q. Tang, X. Fang, C. Zhang, Z. Zhu, Y. Hou, M. Lai, Mater Sci Eng C Mater Biol Appl, 116 (2020) 111241.
[27] S. Ferraris, S. Spriano, Materials Science & Engineering C-Materials for Biological Applications, 61 (2016) 965-978.
[28] Z. Yang, H. Gu, G. Sha, W. Lu, W. Yu, W. Zhang, Y. Fu, K. Wang, L. Wang, ACS Applied Materials & Interfaces, 10 (2018) 41155−41166.
[29] S. Mei, H. Wang, W. Wang, L. Tong, H. Pan, C. Ruan, Q. Ma, M. Liu, H. Yang, L. Zhang, Y. Cheng, Y. Zhang, L. Zhao, P.K. Chu, Biomaterials, 35 (2014) 4255-4265.
[30] Y. Huang, Z. Xu, X. Zhang, X. Chang, X. Zhang, Y. Li, T. Ye, R. Han, S. Han, Y. Gao, X. Du, H. Yang, Journal of Alloys and Compounds, 697 (2017) 182-199.
[31] Y. Huang, S. Han, X. Pang, Q. Ding, Y. Yan, Applied Surface Science, 271 (2013) 299-302.
[32] S.K. Samanta, K.B. Devi, P. Das, P. Mukherjee, A. Chanda, M. Roy, S.K. Nandi, J Mech Behav Biomed Mater, 96 (2019) 227-235.
[33] F. Schmidt-Stein, S. Thiemann, S. Berger, R. Hahn, P. Schmuki, Acta Materialia, 58 (2010) 6317-6323.
[34] S. Liu, Q. Wang, W. Liu, Y. Tang, J. Liu, H. Zhang, X. Liu, J. Liu, J. Yang, L.C. Zhang, Y. Wang, J. Xu, W. Lu, L. Wang, Nanoscale, 13 (2021) 10587-10599.
[35] X. Lu, D. Zhang, W. Xu, A. Yu, J. Zhang, M. Tamaddon, J. Zhang, X. Qu, C. Liu, B. Su, Corros. Sci, 177 (2020) 109007.
[36] A. International, in, 2015.
[37] S. Cui, X. Yin, Q. Yu, Y. Liu, D. Wang, F. Zhou, Corros. Sci, 98 (2015) 471-477.
[38] C. Carlson, S. M. Hussain, A. M. Schrand, L. K. Braydich-Stolle, K. L. Hess, R. L. Jones, J.J. Schlager, The Journal of Physical Chemistry B, 112 (2008) 13608–11361.
[39] W. Xu, A. Yu, X. Lu, M. Tamaddon, L. Ng, M.d. Hayat, M. Wang, J. Zhang, X. Qu, C. Liu, Journal Of Materials Research And Technology, 9 (2020) 9996-10003.
[40] S.A. Alves, A.L. Rossi, A.R. Ribeiro, F. Toptan, A.M. Pinto, J.-P. Celis, T. Shokuhfar, L.A. Rocha, Wear, 384-385 (2017) 28-42.
[41] C.-W. Chan, S. Lee, G. Smith, G. Sarri, C.-H. Ng, A. Sharba, H.-C. Man, Applied Surface Science, 367 (2016) 80-90.
[42] H.-d. Wang, P.-f. He, G.-z. Ma, B.-s. Xu, Z.-g. Xing, S.-y. Chen, Z. Liu, Y.-w. Wang, Journal of the European Ceramic Society, 38 (2018) 3660-3672.
[43] G. Wang, S. Wang, X. Yang, X. Yu, D. Wen, Z. Chang, M. Zhang, Surface & Coatings Technology, 405 (2021) 126512.
[44] A. Mazare, G. Totea, C. Burnei, P. Schmuki, I. Demetrescu, D. Ionita, Corros. Sci, 103 (2016) 215-222.
[45] B. Bozkurt Çırak, S.M. Karadeniz, T. Kılınç, B. Caglar, A.E. Ekinci, H. Yelgin, M. Kürekçi, Ç. Çırak, Vacuum, 144 (2017) 183-189.
[46] Shuxu Wu, Shouren Wang, Wentao Liu, X. Yu, G. Wang, Z. Chang, D. Wen,

Surface & Coatings Technology, 374 (2019) 362–373.
[47] R. Foldbjerg, P. Olesen, M. Hougaard, D.A. Dang, H.J. Hoffmann, H. Autrup, Toxicology Letters 190 (2009) 156-162.
[48] D. Siek, A. Ślósarczyk, A. Przekora, A. Belcarz, A. Zima, G. Ginalska, J. Czechowska, Ceram. Int, 43 (2017) 13997-14007.
[49] D.K. Lee, M.R. Ki, E.H. Kim, C.J. Park, J.J. Ryu, H.S. Jang, S.P. Pack, Y.K. Jo, S.H. Jun, Biomaterial Research, 25 (2021) 2-11.
[50] J. Yu, K. Li, X. Zheng, D. He, X. Ye, M. Wang, PLoS. One, 8 (2013) e57564.
[51] L. Liang, Q. Huang, H. Wu, H. He, G. Lei, D. Zhao, K. Zhou, Journal of Materials Science & Technology, 96 (2022) 167-178.
[52] L. Liang, Q. Huang, H. Wu, Z. Ouyang, T. Liu, H. He, J. Xiao, G. Lei, K. Zhou, Colloids Surf B Biointerfaces, 197 (2021) 111360.
[53] M.H. Kang, S.J. Lee, M.H. Lee, Journal of Ginseng Research, 44 (2020) 823-832.
[54] Y. Ando, H. Miyamoto, I. Noda, N. Sakurai, T. Akiyama, Y. Yonekura, T. Shimazaki, M. Miyazaki, M. Mawatari, T. Hotokebuchi, Materials Science and Engineering: C, 30 (2010) 175-180.
[55] W. Xue, X. Liu, X. Zheng, C. Ding, Biomaterials, 26 (2005) 3455-3460.